

Effect of particle roughness on shear-induced diffusionHan Zhang,¹ Phong Pham,^{1,2} Bloen Metzger ,² Dmitry I. Kopelevich ,¹ and Jason E. Butler ^{1,*}¹*Department of Chemical Engineering, University of Florida, Gainesville, Florida 32611, USA*²*Aix-Marseille University, CNRS, IUSTI 13453 Marseille, France*

(Received 11 October 2022; accepted 25 May 2023; published 16 June 2023)

The shear-induced diffusivity of non-Brownian and neutrally buoyant spheres suspended in a viscous fluid was measured. The monodisperse spheres were roughened using a mechanical process and the diffusions of the original and roughened particles were measured and compared. The rougher particles were found to have a lower diffusivity for volume fractions larger than 0.25, despite expectations that roughness increases diffusion. Simulations that incorporate a contact force predict two regimes of dependence of the diffusion coefficient on roughness: below a volume fraction of 0.2, rougher particles were found to have a larger diffusivity, but a lower diffusivity for volume fractions higher than 0.25. The simulations reveal that increased roughness promotes organization of the concentrated particles into layered structures aligned in the flow direction at high volume fractions. This organization results in fewer particle collisions and a corresponding decrease in the diffusivity. Simulations with and without bounding walls predict similar trends for the diffusion coefficient as a function of volume fraction. Using a sufficiently polydisperse distribution of particle sizes disrupts the organization of the particles and consequently the effect of roughness on diffusivity.

DOI: [10.1103/PhysRevFluids.8.064303](https://doi.org/10.1103/PhysRevFluids.8.064303)**I. INTRODUCTION**

Shearing a suspension of large and neutrally buoyant particles under creeping flow conditions causes individual particles to fluctuate relative to the imposed flow field [1,2]. These seemingly random motions resemble Brownian diffusion, though thermal fluctuations of the particles are negligible. This shear-induced diffusion of particles drives associated fluctuations in the fluid, which can be used to enhance mixing and heat transfer [3–6] in viscous fluids. The diffusion of particles is also closely related to the shear-induced migration of particles in inhomogeneous shearing flows [7,8]. These net migrations of particles can cause erroneous measurements of the effective viscosity of suspensions [9,10] and an overprediction of the pressure drop needed to pump a viscous suspension through a conduit at a fixed volumetric flow rate [11,12].

The practical impact of shear-induced diffusion on the more general dynamics of suspension flows has motivated multiple investigations. Scaling analysis [2,13] suggests that the diffusivity is proportional to the rate of shear ($\dot{\gamma}$) and squared diameter (d^2) of the spheres, as confirmed in experiments. However, measurements of the diffusion coefficient [1,2,5,13–16] show a wide range of values, particularly at the larger volume fractions, ϕ , as seen in Fig. 1.

Some of the discrepancies between measurements have been attributed to differences in experimental capabilities. For example, Leighton and Acrivos [2] noted that the time of observation must be sufficiently short in order to ensure that bounding walls do not influence the results. Analysis they performed indicated that the measurements of Eckstein *et al.* [1] at high volume fractions ($\phi \geq 0.3$)

*butler@che.ufl.edu

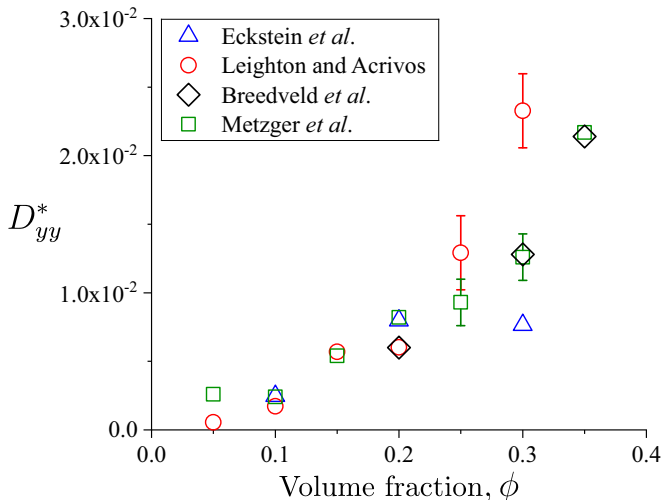


FIG. 1. Experimental results for the dimensionless diffusivity in the gradient direction ($D_{yy}^* = D_{yy}/\dot{\gamma}d^2$) as a function of the particle volume fraction, ϕ , where $\dot{\gamma}$ is the rate of shear and d is the particle diameter. The data has been collected from previous works as noted in the legend.

were likely affected by the walls. The time of observation also must be sufficiently large to ensure that the mean-square displacement attains its steady, diffusive value [15,17].

Properties of the suspension might also be responsible for differences in the observations. The studies shown in Fig. 1 took care to utilize Newtonian fluids and particles of large and monodisperse size. However, a conspicuous variable is the rugosity of the particles used in the different experiments. Evidence that roughness alters the dynamics of particles colliding in shear flows includes detailed studies of the asymmetry of the pair probabilities [18–20]. More recently, experiments demonstrated that particle roughness impacts the loss of reversibility [21] and the transition from a reversible to irreversible state [22]. Also, analysis [23] of interactions between particle pairs colliding in a shear flow predicts that particle roughness increases the net displacement across streamlines. Consequently, the shear-induced diffusivity is expected to be larger for particles that are rougher.

Despite expectations, experimental results presented in Sec. IV indicate that rougher particles have a lower diffusivity than smooth particles for volume fractions greater than 0.25. These experimental results are confirmed by simulations, which further reveal a nonmonotonic trend of the diffusivity with the roughness: diffusivity first increases with roughness at volume fractions below 0.20 as predicted in the dilute limit. Then, diffusivity decreases with roughness for volume fractions larger than 0.25. In this paper, the latter result is shown to arise from a strong effect of the roughness on the microstructure. As explained in Sec. VB 1, rougher particles organize more strongly into layers that align in the flow direction at high concentrations. This layered structure enables roughened particles to pass by one another without colliding, which decreases the diffusivity relative to smoother particles.

II. EXPERIMENTS

A. Particles and fluid

Experiments were performed at volume fractions of $\phi = 0.25, 0.3, \text{ and } 0.35$ and using two different batches of particles having different roughness. Highly uniform spheres of diameter $d = 2.00 \pm 0.01$ mm were used in all of the experiments. The particles were composed of polymethyl methacrylate (Engineering Laboratories Inc.). To explore the effect of surface roughness on

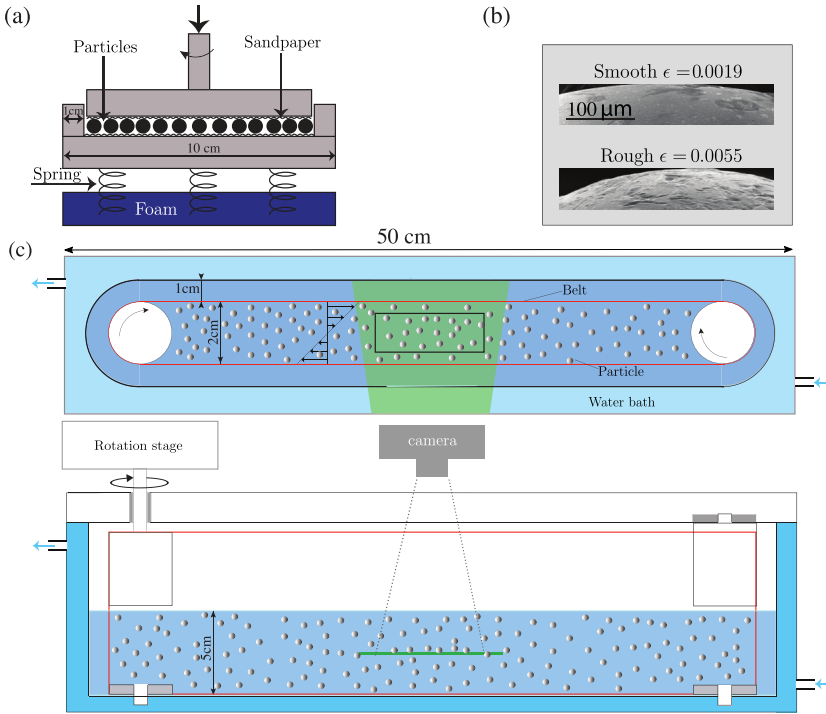


FIG. 2. (a) Particles were roughened between two plates covered with sandpaper. The top plate was rotated using a motor while a normal force was applied; the bottom plate, resting on a foam support to prevent jamming, was prevented from rotating. (b) Sample images from scanning electron microscopy of a smooth and roughened particle. (c) Sketches of the experimental shear cell from a top and side perspective. A linear shear flow was generated by rotating the transparent belt (in red). The suspension (dark blue fluid and particles) was added to the space between the belts to a depth of 5 cm and suspending fluid (only) filled the space between the belt and the wall of the shear cell. Water (light blue) at 22 °C circulated through the jacket surrounding the shear cell. A laser sheet (green) fluoresced the fluid to enable visualization of the particles, which were otherwise indistinguishable from the fluid. The black rectangle indicates the window of observation.

the particle dynamics, particles were roughened between two sandpaper sheets under a confining pressure as illustrated in Fig. 2(a). Both the top and bottom plates were covered with sandpaper having grit size P60. The top plate was rotated for 10 min at 130 rpm, while the bottom plate was held stationary by a thick foam support, which also acted as a spring to prevent jamming. Several particle samples, both before and after roughening, were imaged using scanning electron microscopy. The smooth (new) particles had an average peak roughness of $\epsilon d = 3.8 \pm 2.8 \mu\text{m}$ and the roughened particles had an average peak roughness of $\epsilon d = 11.0 \pm 6.0 \mu\text{m}$. Figure 2(b) shows a sample image of a smooth and roughened particle.

The suspending fluid was a mixture of Triton X-100 (73.9% by weight), zinc chloride (14.2%), and water (11.9%). Trace amounts of hydrochloric acid, to prevent the formation of zinc hypochloride precipitate, and Rhodamine 6G, a fluorescent dye, were added to the fluid as well. The density and refractive index of this suspending fluid matched that of the particles at a temperature of 22 °C. The mixture is a Newtonian fluid with a viscosity of $\mu = 3 \text{ Pa s}$ and a density of $\rho = 1.19 \text{ g/cm}^3$.

B. Shearing geometry

The suspension was sheared in the custom-built cell illustrated in Fig. 2(c). The shear cell was composed of two vertical cylinders, around which a transparent belt made of polymethyl

methacrylate was wrapped. Rotating the cylinders, using a high precision rotating stage (M-061.PD from PI piezo-nano positioning), generated a linear shear flow between the translating belt and far from the cylinders. The diameter of the cylinders, and hence gap between the belts, was $H = 2$ cm, allowing the use of relatively large particles in the experiments while still having a large gap to particle size of $H/d = 10$. The spacing between the belt and the outer wall of the shearing cell was 1 cm at every point around the perimeter of the device; this constant spacing minimized unwanted, secondary flows. A water bath surrounding the shear cell maintained the system at 22°C to ensure that the refractive index of the particles and fluid remained well matched.

This shearing cell was identical to that used by Pham *et al.* [22], but a steady shear flow was utilized here instead of an oscillatory one. The experiments were performed with a maximum rate of shear of $\dot{\gamma} = 0.1 \text{ s}^{-1}$; hence the Reynolds number was $\dot{\gamma}\rho H^2/\mu = 0.016$ (or $\dot{\gamma}\rho d^2/\mu = 1.6 \times 10^{-4}$ if using the particle scale) at most and the Péclet number ($\dot{\gamma}\mu d^3/8k_bT$) was very large (up to 7.5×10^{10}).

C. Imaging and image analysis

Illumination provided by a green laser diode (2 W power and wavelength of 532 nm) was used to fluoresce a sheet of the fluid of $\approx 60 \mu\text{m}$ thickness. The laser sheet was positioned 2.5 cm below the free surface of the suspensions. The window of observation was about 6.8 cm long (34 particle diameters) in the flow direction, 1.7 cm wide (8.5 particle diameters) in the gradient direction, and was centered between the belts and the cylinders, as indicated by the black rectangle in Fig. 2(c).

Particles within the plane of the laser sheet were imaged from above the shear cell using a Nikon D300s camera with a magnification lens (Sigma APO-Macro-180mm-F3.5-DG). To prevent photobleaching of fluid due to the high power laser source, an optical beam shutter (SH05 Shutter ThorLabs) was mounted in front of the laser. The shutter and camera, as well as the rotating stage that controls the rate of shear, were actuated automatically using a custom control system.

The index-matched suspension was transparent, but fluid within the horizontal laser sheet appeared bright due to the presence of the fluorescent Rhodamine 6G; the particles within the laser sheet appeared as black disks [see Fig. 3(a)]. Note that all particles have the same diameter and the apparent size differences arise from the relative, vertical position of the laser sheet and the particles. The images were collected and then analyzed using a distance transform to identify the positions of the particles, as shown in Fig. 3(b). A description of the image analysis method is in Sec. S5 of the Supplemental Material [24].

D. Determination of the particle diffusion coefficient

To initiate an experiment, the suspension of the desired volume fraction was poured into the shear cell and was mixed by shearing back and forth at a large strain amplitude of 30 for 2 h. Then the suspension was sheared continuously for a total strain of 20 while images were collected at every strain interval of 0.1. The small strain amplitude between successive images enabled tracking of individual particles during the course of an experiment, from which trajectories were constructed. Figure 3(c) shows a sample set of trajectories for the individual particles. Ten experiments were done for each volume fraction and particle type (smooth and roughened).

From the particle positions as a function of the strain (i.e., the trajectories), the displacement $\Delta y(\gamma) = y(\gamma + \gamma_0) - y(\gamma_0)$ of each particle in the gradient (y) direction was measured, where $\gamma_0 = 0$ was the strain at which the observation was initiated and γ was the strain over which the observation was made. Note that the displacements are driven only by shear, not by thermal fluctuations, and no external forces act on the particles. So the particle displacements are strictly a function of the strain $\gamma - \gamma_0$, which is related to the elapsed time t through the steady shear rate by $\dot{\gamma} = (\gamma - \gamma_0)/t$. The displacements were used to calculate the mean-square displacements as a function of the strain, $\langle \Delta y \Delta y \rangle(\gamma)$, where the brackets indicate an average over all particles and experiments for the volume fraction and particle type of interest. At sufficiently large strains, the

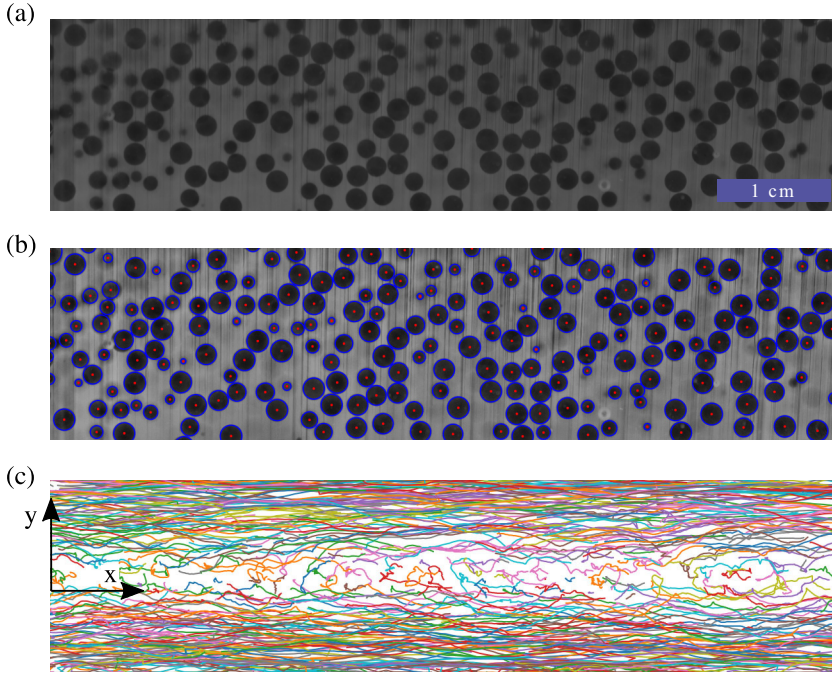


FIG. 3. (a) Sample image of the suspension within the shearing cell at a volume fraction of 0.35 for the case of rough particles ($\epsilon = 0.0055$); the fluid appears bright due to fluorescence, while the particles appear black. (b) Particles detected within the sample image using the distance transform algorithm are marked with blue circles and their centers are marked with red dots. (c) Successive images were used to construct the trajectory of individual particles, as represented by the lines. As indicated, x is the direction of flow and y is the gradient direction. Note that roughening the particles does not degrade the image quality nor the ability to track particles (see Sec. S5 of the Supplemental Material [24] for more information and additional images from the experiments).

mean-square displacements are generally presumed to grow linearly with the strain and the gradient component of the diffusion, D_{yy} , can be defined by

$$\langle(\Delta y)^2\rangle = \frac{2D_{yy}}{\dot{\gamma}}\gamma. \quad (1)$$

Since the diffusivity scales with the rate of shear and the square of the particle size, it is reported in dimensionless form as $D_{yy}^* = D_{yy}/\dot{\gamma}d^2$.

The diffusive regime can be difficult to measure experimentally due to the inability to track particle positions over large strain intervals. One issue is that particles disappear from the field of view during an experiment, while another concern is that the displacements due to diffusion can become comparable to the spacing of the shearing walls [2]. Also, walls can lead to abnormally high rates of diffusion for dilute suspensions [16,25] and numerical simulations [26] indicate that walls can cause deviations from diffusive dynamics for concentrated suspensions. For the experimental setup described here, the particle positions could be tracked for strains of up to 10 without disappearing from the viewing window and the wall spacing was still large compared to the diffusion length over this strain. This is an improvement compared to other experiments where the particle positions were followed continuously in time, such as those of Breedveld *et al.* [13] and Metzger *et al.* [5], where the maximum tracking strain was 3.5 and 7, respectively. To calculate the diffusion coefficient from the experimental results, the mean-square displacement was fit to

Eq. (1) over the range $\gamma = 4$ to 10 (see also Sec. S2 [24] for more information). Only the gradient component of the diffusivity was evaluated.

III. SIMULATIONS

Simulations were used to evaluate the effects of roughness on hydrodynamic diffusivity for a range of conditions. The model used for the simulations is described in the next section. Details about the numerical implementation and quantifications of the predicted microstructures are given in Secs. III B and III C.

A. Model equations

The model balances the hydrodynamic forces, \mathbf{F}_i^h , with contact forces that represent the influence of the roughness,

$$\mathbf{F}_i^h + \sum_{j \neq i}^N \mathbf{F}_{ij}^c = 0, \quad (2)$$

for each particle i of the N total particles; the contact force on a particle i due to another particle j is \mathbf{F}_{ij}^c . The balance ignores inertial effects and Brownian fluctuations, consistent with the low Reynolds numbers and large Péclet numbers in the experiments.

The hydrodynamic forces are approximated by the sum of the drag due to the background shear flow and the normal components of the lubrication interactions between neighboring particles,

$$\mathbf{F}_i^h = 3\pi\mu d_i(\dot{\mathbf{x}}_i - \dot{\gamma}y_i\boldsymbol{\delta}_x) + \sum_{j(i)} \frac{3\pi\mu d_i^2 d_j^2}{2h_{ij}(d_i + d_j)^2} \mathbf{n}_{ij}(\dot{\mathbf{x}}_i - \dot{\mathbf{x}}_j) \cdot \mathbf{n}_{ij}, \quad (3)$$

where \mathbf{x}_i is the position of particle i and $\dot{\mathbf{x}}_i$ is its velocity. The drag force is proportional to the diameter d_i of particle i and depends upon the particle velocity relative to the shear flow in the x direction, with gradient in the y direction. The unit vector in the x direction is $\boldsymbol{\delta}_x$. The second term in Eq. (3) represents the lubrication forces between particle i and the particles $j(i)$ located within the lubrication range of particle i . These forces depend upon the relative velocities of each pair and their separation distance $h_{ij} = |\mathbf{x}_{ij}| - 0.5(d_i + d_j)$, where $\mathbf{x}_{ij} = \mathbf{x}_i - \mathbf{x}_j$ and $|\mathbf{x}_{ij}|$ is its magnitude. The set of particles $j(i)$ that are located within the lubrication range of particle i satisfy the constraint that $\epsilon(d_i + d_j) < h_{ij} \leq (d_i + d_j)/4$, where ϵ denotes the dimensionless roughness of the particles. The model only accounts for the normal component of lubrication [27], which acts along the normal vector $\mathbf{n}_{ij} = \mathbf{x}_{ij}/|\mathbf{x}_{ij}|$.

The contact forces in Eq. (2) are modeled using the simple form

$$\mathbf{F}_{ij}^c = \begin{cases} F_0 \hat{F}_0 \mathbf{n}_{ij} & \text{if } h_{ij} \leq \epsilon(d_i + d_j), \\ 0 & \text{if } h_{ij} > \epsilon(d_i + d_j), \end{cases} \quad (4)$$

where $F_0 = 6\pi\mu(d/2)^2\dot{\gamma}$ is the characteristic force, $\hat{F}_0 = 20$ is the dimensionless amplitude of the repulsive force, and d is the average particle diameter. Note that lubrication interactions are not applied to a particle pair once the repulsive force activates [i.e., when $h_{ij} \leq \epsilon(d_i + d_j)$]. For simulations where bounding walls are present, a force of $F_0\hat{F}_0$ is applied on each particle i within a distance of $(0.5 + \epsilon)d_i$ in the normal direction to the wall in order to prevent overlaps.

This model is similar to the one used in previous works where more details can be found [21,28]. The model does not include long-range hydrodynamic interactions, as they are not responsible for the irreversible motion of the neutrally buoyant particles [29], nor are tangential lubrication interactions or friction included in the model. However, as demonstrated in Sec. S1 [24], the model correctly predicts many key elements of the suspension properties, including the pair distribution function.

B. Numerical implementation

Equations (2), (3), and (4) form a set of coupled ordinary differential equations that were solved for the velocities of the particles from their instantaneous spatial positions. The positions were updated in time using a fourth-order Runge-Kutta integrator while ensuring a particle displacement of less than $5 \times 10^{-3}d$ per step. Most simulations used a monomodal particle size ($d_i = d$ for $i = 1$ to N), but a polydisperse distribution of particle sizes was used for results presented in Sec. VB3. Simulations were performed in three dimensions and for monolayers, where the particles' centers were initially placed, and remained, on a plane spanning the flow and gradient directions. Initial positions of the N particles were assigned from a uniform random distribution by placing each particle sequentially within the simulation domain while ensuring a nonoverlapping configuration. All of the simulation results reported here employed periodic conditions in the flow and vorticity (for fully three dimensional cases) directions, where the boundaries were separated by a distance of $L = 10d$ in both directions. The gradient direction was bounded by impermeable walls separated by a distance of $10d$ in most simulations in order to match the experimental conditions. However, some simulations were performed with different wall spacings or fully periodic boundary conditions [30]. In those cases where periodic boundary conditions were used in the gradient direction, the spacing was set to $10d$. Tests verified that these domain sizes were sufficient to provide results that were independent of the box sizes.

After assigning the distribution, the system was sheared backwards and then forwards for a strain of 20 in each direction prior to beginning the tracking of particle positions at $\gamma = 0$. Steady shear, continuing in the same direction, was then performed for a total strain of at least 40. The diffusivity coefficient, D_{yy}^* , was calculated using Eq. (1) using strains of $\gamma = 4$ to 10, for comparing to experimental results, as well as over strains $\gamma = 20$ to 40.

C. Characterization of suspension microstructure

Microstructures predicted by monolayer simulations are reported in Sec. V. Three different quantifications were used: the particle density profiles in the gradient (y) direction, the structure factor, and the angular pair distribution function. Note that some additional measures of microstructure are presented in Secs. S3 and S4 [24].

To explore lateral organization of the suspension, the average concentration was computed as a function of y . The system was divided into bins of equal size b in the gradient direction (from the top to bottom boundaries). For each bin, areas of particle segments contained within the bin were summed and then divided by the bin area Lb to give $\phi(y)$. The area fraction profile $\phi(y)$ was then averaged over all of the system configurations with strains between 20 and 40 and over all simulation runs to give $\langle \phi_y \rangle$.

The average area fraction profile $\langle \phi_y \rangle$ is suitable for analysis of particle structures in bounded systems of relatively small size ($H/d \leq 10$). However, in unbounded or large bounded systems, $\langle \phi_y \rangle$ can falsely indicate a uniform distribution due to random phase shifts in the particle density far from the walls. Such shifts are less likely in small bounded systems, since the phase of the particle density in these systems is determined by walls.

To eliminate the effect of the phase shift, the spectral intensity of the particle density was calculated by Fourier transforming the point density,

$$\rho(y) = \frac{1}{N} \sum_{j=1}^N \delta(y - y_j), \quad (5)$$

of the particle centers y_j , since in a monodisperse suspension, the area fraction $\phi(y)$ is related to the point density by a convolution

$$\phi(y) = \int_0^H a(y - y') \rho(y') dy'. \quad (6)$$

Here, $a(y)dy$ is the area of a differential segment of a particle, with the particle centered at $y = 0$ and the segment located in the range $[y, y + dy]$. The Fourier transform of the particle density (5) is

$$\hat{\rho}(q_y) = \frac{1}{H} \int_0^H \rho(y) e^{-iq_y y} dy = \frac{1}{HN} \sum_{j=1}^N e^{-iq_y y_j}, \quad (7)$$

where q_y is the wave number in the lateral direction. The spectral intensity $\langle |\hat{\rho}(q_y)|^2 \rangle$ is directly related to the structure factor

$$S(\mathbf{q}) = \frac{1}{N} \sum_{j,k} \langle e^{i\mathbf{q} \cdot (\mathbf{r}_j - \mathbf{r}_k)} \rangle, \quad (8)$$

where $\mathbf{q} = (q_x, q_y)$ is the wave vector. Specifically,

$$\langle |\hat{\rho}(q_y)|^2 \rangle = \frac{1}{H^2 N} S(0, q_y). \quad (9)$$

In this paper, $S = S(0, q_y)$ is used to assess the suspension microstructure in the gradient direction.

The angular pair distribution function, $g(\theta; \delta)$, is the probability density of finding a pair of particles having angle θ within a given range of distances, $d \leq r < d(1 + \delta)$, near contact. Here, the angle θ is measured from the flow direction and 0° to 90° corresponds to the compressional quadrant. The pair distribution function $g(\theta; \delta)$ was normalized so that its integral over θ is 1 and the value of δ was set to 0.05. The Fourier transform of the pair distribution function $g(\theta; \delta)$ is directly related to the structure factor S . However, both S and $g(\theta; \delta)$ are reported within Sec. V since $g(\theta; \delta)$ provides an assessment of the local microstructure of the suspension near particle contact.

IV. RESULTS

Section IV A focuses on the experimental results and the results of simulations in three dimensions are given in Sec. IV B. Section V contains results from simulations of a monolayer of particles which are used to both explain and expand upon the experimental observations.

A. Experiments at large ϕ

Figure 4(a) shows the mean-square displacements in the gradient direction as measured experimentally for $\phi = 0.25$ and 0.35 for the smooth and roughened particles. The mean-square displacements are larger for the higher volume fraction, as generally expected. Additionally, the mean-square displacements for the smooth particles are significantly larger than for the rough particles at $\phi = 0.35$.

The measurements of the mean-square displacements over the range of $\gamma = 4$ to 10 were fit to Eq. (1). This choice does not have a significant impact on the resulting diffusivity as indicated in the Supplemental Material [24]. Also in Sec. S2 [24], it is noted that the mean-squared displacement deviates from the diffusive scaling for the smaller volume fractions of 0.25 and 0.30 . This is observed in both experiments and simulations. However, throughout this paper we fit the mean-square displacement to a linear function of strain in order to compare particle dynamics at varying conditions. Figure 4(b) shows the resulting diffusivities, D_{yy}^* , for the three volume fractions and two values of roughness that were measured. The smoother particles were found to have a larger diffusivity than the roughened ones for volume fractions higher than 0.25 .

B. Simulations in three dimensions

Figure 5 shows the mean-square displacements and diffusivities calculated using fully three-dimensional simulations and conditions matching those in the experiments. Error bars for the diffusivities in Fig. 5(b), as well as for all other reported diffusivities from simulations, indicate the standard deviation of the mean values from each simulation run. Standard deviations are shown

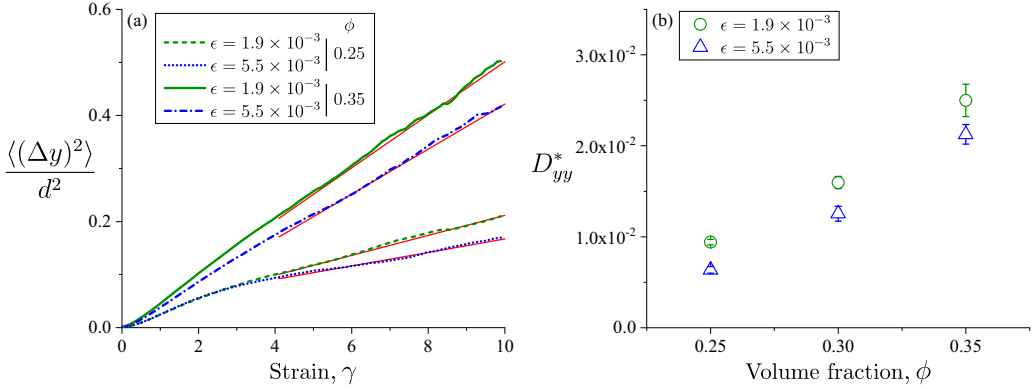


FIG. 4. Experimental measurements. (a) Average mean-square displacements in the gradient direction, $\langle\Delta y\Delta y\rangle/d^2$, versus strain, γ , for experiments at volume fractions of 0.25 and 0.35 and two different values of roughness, ϵ . (b) Diffusion coefficient as a function of volume fraction and roughness calculated from the displacements for strains of $\gamma = 4$ to 10, as indicated by the red lines in (a). The error bars indicate the standard error of the mean value from the ten experiments that were performed for each condition.

instead of standard errors, as for the experimental measurements, since the standard errors from the simulations are too small to see on the plots.

Consistent with the experiments, the rougher particles are less diffusive than the smoother ones at $\phi = 0.35$. These outcomes remain true whether fitting the mean-square displacements over a range of $\gamma = 4$ to 10, as in the experiments, or over a range of $\gamma = 20$ to 40, as indicated by the lines in Fig. 5(a). The experimental diffusivities in Fig. 4(b) are comparable in magnitude to those of previous works at similar volume fractions, as seen in Fig. 1. However, the diffusivities observed from simulations in Fig. 5(b) are substantially smaller than the experimentally determined diffusivities [Fig. 4(b)], despite having qualitative similarities. Similar, quantitative discrepancies between experiments and simulations have been noted in many other works [5,13,14].

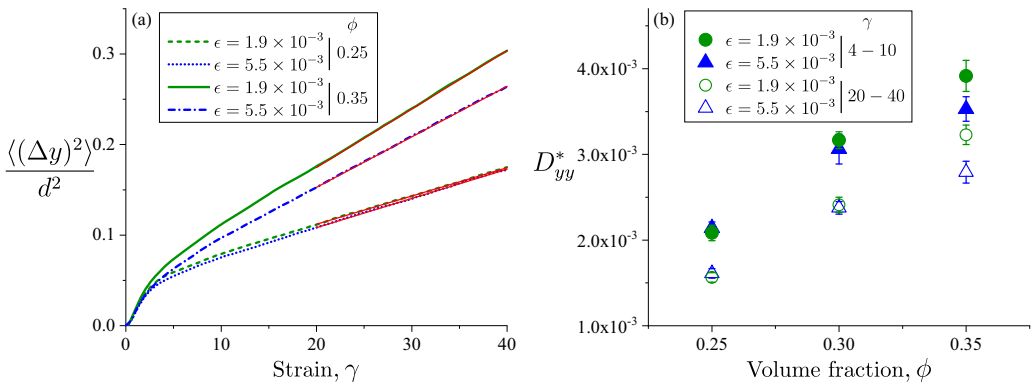


FIG. 5. Simulation results in three dimensions are shown for values of ϕ , ϵ , and $H/d = 10$ matching the experimental conditions. (a) Average mean-square displacements in the gradient direction, $\langle\Delta y\Delta y\rangle/d^2$, versus strain, γ . (b) Diffusion coefficients calculated from mean-square displacements between $\gamma = 4$ and 10 and also from mean-square displacements between $\gamma = 20$ and 40, where the latter is indicated by red lines in (a). Data on particle displacements were collected from a window of width $8.5d$ centered between the bounding walls in order to mimic the experimental measurements. The error bars indicate the standard deviation.

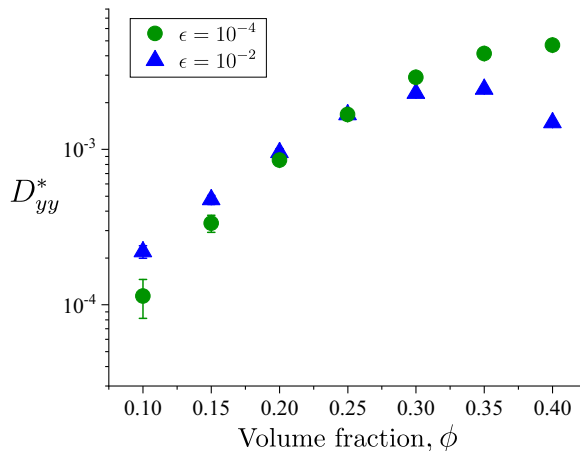


FIG. 6. Dimensionless diffusion coefficient predicted by three-dimensional simulations with $H/d = 10$. The diffusion coefficient was calculated from mean-square displacements for strains of $\gamma = 20$ to 40.

Experiments could not be performed for small concentrations owing to the inability to track particles over a sufficiently large strain in order to ensure attainment of the diffusive regime. Instead, simulations were used to explore the effect of roughness on the diffusion coefficient for a wide range of volume fractions of $\phi = 0.1$ to 0.4. Figure 6 shows the diffusion coefficient calculated from the mean-square displacements over the range $\gamma = 20$ to 40. Two regimes of diffusivity are observable.

For low ϕ , increasing roughness increases the diffusivity as anticipated [23]. However, at large ϕ , the opposite trend is observed: as measured experimentally [Fig. 4(b)], increasing roughness decreases the diffusivity.

V. ANALYSIS

Within this section, the effect of roughness on the shear-induced diffusivity is correlated to previous theories at low ϕ and to changes in the microstructure at high ϕ . To achieve this, monolayer simulations were performed since they are simpler to analyze, save significant computational time, and enable the exploration of a wide range of conditions while maintaining the same, relevant physics.

As an example, Fig. 7(a) reports the diffusivities as a function of the areal fraction, $\phi_A = N\pi d^2/4HL$. The results confirm the trends seen in the experiments [Fig. 4(b)] and simulations in three dimensions (Fig. 6): as compared to smoother particles, rougher particles diffuse faster at low concentration and slower at high concentrations. This is reemphasized in Fig. 7(b), where diffusivities are reported for $\epsilon = 10^{-4}$ to 5×10^{-2} at three different areal fractions ($\phi_A = 0.15, 0.25$, and 0.45). At $\phi_A = 0.25$, particle roughness has little impact on the diffusion. Diffusivity decreases as particle roughness increases for $\phi_A = 0.45$, but increases with roughness for $\phi_A = 0.15$.

A. Low ϕ_A range

The larger diffusivity of rougher particles observed at low concentrations can be explained simply by considering two-body interactions. Figure 8(a) illustrates the relative trajectory between two particles located in the shear-gradient plane and plotted in the reference frame of particle 1, where $x' = [x_2(t) - x_1(t)]/d$ and $y' = [y_2(t) - y_1(t)]/d$. Figure 8(b) shows the final offset Δy^∞ obtained when varying the particle roughness ϵ , for three values of the initial offset Δy^0 . For a given initial offset Δy^0 , when the particle roughness is small enough, particles do not make solid contact. In this case, the particle relative trajectory is symmetric yielding $\Delta y^\infty = \Delta y^0$, as shown by the two plateaus

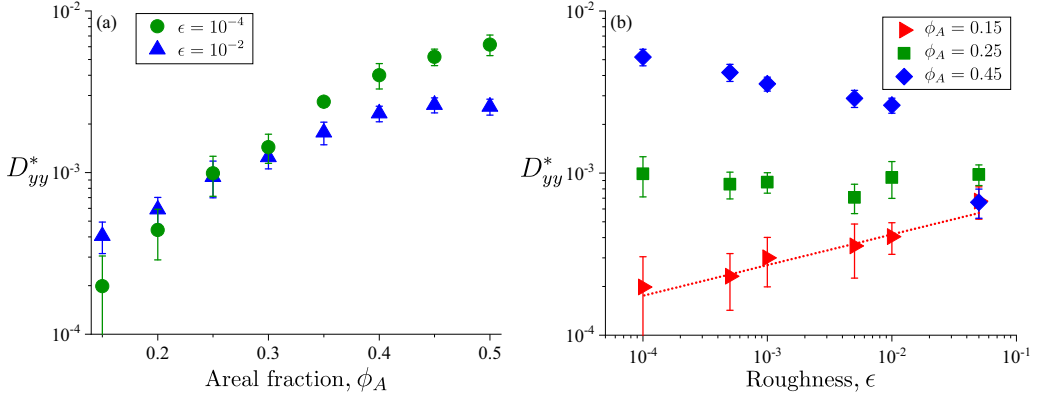


FIG. 7. Results of diffusivities from monolayer simulations with $H/d = 10$. (a) Dimensionless diffusion coefficient versus areal fraction ϕ_A for two values of particle roughness. (b) Dimensionless diffusion coefficients versus particle roughness for $\phi_A = 0.15, 0.25$, and 0.45 . The red line shows $D_{yy}^* = 1.0 \times 10^{-3} \epsilon^{0.19}$, which is the power law fit of D_{yy}^* to ϵ for $\phi_A = 0.15$.

in Fig. 8(b). Conversely, above a certain roughness, particles make solid contact and the final offset then varies with the particle roughness, which sets the separation distance between the particles at the apex of their interaction (i.e., when $x_1 = x_2$). The final offset for particle pairs that contact can be closely fitted by $\Delta y^\infty = 1.585\epsilon^{0.251}$ [red line in Fig. 8(b)], suggesting that $\Delta y^\infty \propto \epsilon^{1/4}$. Note that this curve can also be interpreted as the minimum separation distance (ϵ) reached by smooth particles that have an offset Δy^∞ when they are infinitely separated.

The above scaling relation between the final offset and the particle roughness is of interest for two reasons. First, in the dilute limit when two-body interactions are dominant, it provides a simple way to estimate the particle roughness from pair distribution functions. For instance, by measuring the offset position of the “high concentration tail” in the pair distribution measured by Blanc *et al.* [31] for a suspension of volume fraction $\phi = 5\%$ and by using the above relation, a roughness of $\epsilon d = 272$ nm can be estimated for their particles, whereas they reported a peak roughness of approximately 200 nm. This data point is included in Fig. 8(b). Second, in the same limit, this

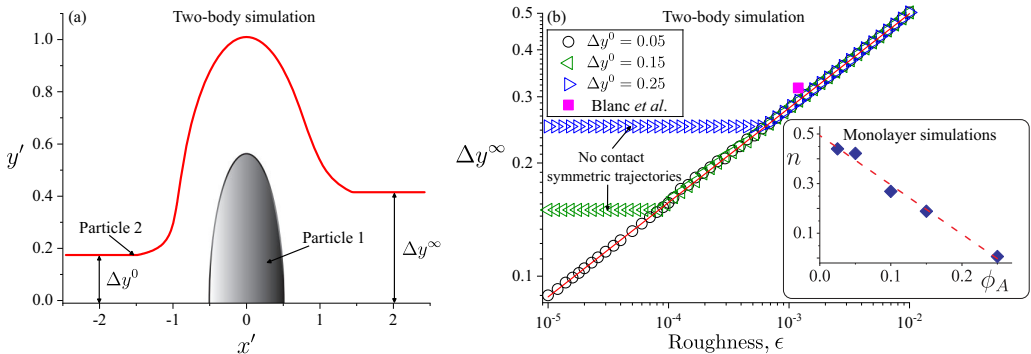


FIG. 8. (a) Two-body simulation showing the relative trajectory during a collision between two particles of roughness $\epsilon = 0.005$. (b) Two-body simulation showing the final offsets, Δy^∞ , versus particle roughness, ϵ , for three different initial offsets Δy^0 . Red line: $\Delta y^\infty = 1.585\epsilon^{0.251}$. Inset: exponent n obtained from monolayer suspension simulations by fitting the diffusion coefficient to $D_{yy}^* \propto \epsilon^n$ for different volume fractions, as shown in Fig. 7(b) for $\phi_A = 0.15$. The linear extrapolation of n to $\phi_A = 0$ yields $n = 0.49$.

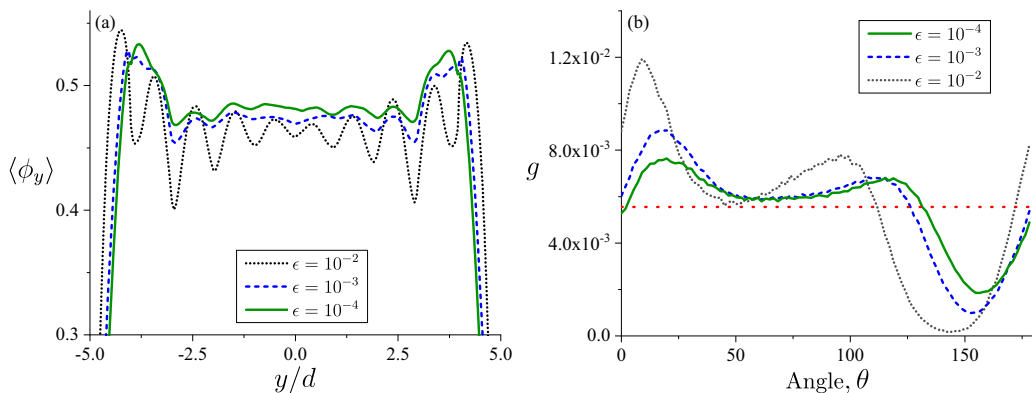


FIG. 9. (a) Average local areal fraction, $\langle \phi_y \rangle$, and (b) angular pair distribution, $g(\theta; \delta)$ with $\delta = 0.05$. The results are from monolayer simulations at $\phi_A = 0.45$ and $H/d = 10$ for three values of ϵ . Data was collected for strains $\gamma = 20$ to 40 . The dashed red line in (b) indicates the average value of $g(\theta; \delta)$.

relation implies that the particle diffusion coefficient in homogeneous suspensions should depend on the particle roughness, as mentioned in previous studies [23]. Estimating the typical collision rate between particles as $\tau \sim 1/(\dot{\gamma}\phi_A)$ and the particle transverse displacement after each collision by $l = \Delta y^\infty d/2$, one can predict that the diffusion coefficient should scale as $D_{yy} \propto l^2/\tau \propto \phi_A \epsilon^{1/2} \dot{\gamma} d^2$.

To test whether the above scaling, obtained from considering two-body interactions, applies in homogeneous suspensions, monolayer simulations were performed at low area fractions by systematically varying the particle roughness ϵ between 10^{-4} and 10^{-1} . Figure 7(b) shows that for $\phi_A = 0.15$ the diffusion coefficient versus ϵ can be well fitted $D_{yy}^* \sim \epsilon^n$ with $n = 0.19$. Similar fits were performed for ϕ_A ranging from 0.025 to 0.25 and the inset of Fig. 8(b) reports the values of the exponent n . By linearly extrapolating these results to $\phi_A \rightarrow 0$, homogeneous simulations recover $D_{yy} \sim \epsilon^{0.49}$, in close agreement with the predicted scaling of $D_{yy} \sim \epsilon^{1/2}$ obtained above by considering only two-body interactions.

B. High ϕ_A range

The dependence of the diffusivity on particle roughness qualitatively changes once the volume fraction surpasses 0.25. As shown in Fig. 7, smoother particles diffuse more than rougher ones. In the following, this trend is correlated with changes in the microstructure as evaluated from particle density profiles and angular pair distributions for smooth and rough particles. Also, the influence of the bounding walls and polydispersity are examined in Sec. VB 2 and Sec. VB 3.

1. Suspension microstructure

Figure 9(a) shows the local concentration $\langle \phi_y \rangle$ of particles as a function of the y position for three different roughnesses at $\phi_A = 0.45$. Particle centers are excluded from accessing regions within one radius ($d/2$) of the bounding walls located at $y/d = \pm 5.0$ and there is a peak in the value of $\langle \phi_y \rangle$ near each bounding wall which corresponds to a layer of particles that is aligned in the direction of flow. These features of the particle distribution are seen in other works [32,33] and occur for all values of ϵ studied here.

However, strong differences that depend on the roughness are seen in the local concentration upon moving away from the bounding walls. The local areal fraction is flat and unstructured for small particle roughness ($\epsilon = 10^{-4}$), indicating that the layering disappears. However, at a large roughness ($\epsilon = 10^{-2}$), $\langle \phi_y \rangle$ demonstrates a regular, periodic oscillation throughout the channel and with peaks spaced at a distance of d . The result indicates that the rougher particles align in the flow direction throughout the system.

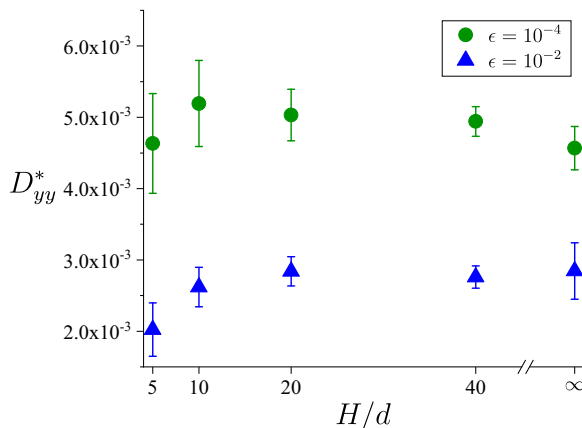


FIG. 10. Diffusivity as a function of confinement for $\phi_A = 0.45$ and two values of ϵ . Results are shown for bounded simulations with $H/d = 5$ to 40 and also for periodic boundaries in the gradient direction ($H/d = \infty$).

More evidence that roughness promotes particle alignment is given by the angular pair distribution, $g(\theta; \delta)$, as shown in Fig. 9(b). The angular pair distributions are evaluated over strains of $\gamma = 20$ to 40 and results are presented for angles $0^\circ < \theta < 180^\circ$. Consistent with other works [32,34], the pair distribution shows an excess of particle pairs in the compressional quadrant which spans $0^\circ < \theta < 90^\circ$. For large particle roughness ($\epsilon = 10^{-2}$), the angular pair distribution shows a large excess of particles behind ($\theta = 180^\circ$) and in front of ($\theta = 0^\circ$) each other, which is not seen for the smoother particles where $g(0^\circ)$ and $g(180^\circ)$ are roughly equivalent to the mean value of $g(\theta) = 1/180$. This indicates that rougher particles are layering more strongly than smoother particles.

Metzger *et al.* [28] have previously shown, using a simulation model similar to that used here, that particles organize into flow aligned layers when lubrication forces are screened. Here, simulations demonstrate that increasing the roughness, and consequently weakening the role of lubrication interactions, also drives an alignment of particles in the flow direction. Stronger flow alignment of particles reduces the rate of collision, as the particles can pass by one another without colliding, and hence lowers the diffusivity. The less organized structure obtained for relatively smooth particles results in a higher frequency of collisions and a larger diffusivity, even though the net displacement associated with each collision is smaller for the smoother particles.

Also, note that changes in the structure that lead to differences in the diffusivities are small unless either the volume fractions or differences in the roughnesses are large according to simulations. Consequently, for the case studied experimentally that gives the biggest difference in diffusivities ($\phi = 0.35$ with $\epsilon = 1.9 \times 10^{-3}$ versus 5.5×10^{-3}), changes in the structure are not detected within the images as discussed in Sec. S5 of the Supplemental Material [24].

2. Effect of confinement

The strong layering that is observed at large volume fractions could be due to the boundaries, as all results shown in Figs. 4–9 have been limited to a single confinement ratio of $H/d = 10$. Consequently, simulations were performed with bounding walls up to $H = 40d$, as well as with periodic boundary conditions in the gradient direction with a period of $10d$. Results for the diffusivities are shown in Fig. 10 at an areal fraction of 0.45 for relatively smooth ($\epsilon = 10^{-4}$) and rough ($\epsilon = 10^{-2}$) particles. The fully periodic simulations are located at $H/d = \infty$ on the graph.

The diffusivities change little for confinements of $H/d > 5$ for both values of ϵ , consistent with results regarding the more general dynamics and rheology of suspensions of non-Brownian spheres [33,35]. The simulations also indicate that the smooth particles consistently have higher diffusivity than the rough particles, independent of confinement, for this high volume fraction.

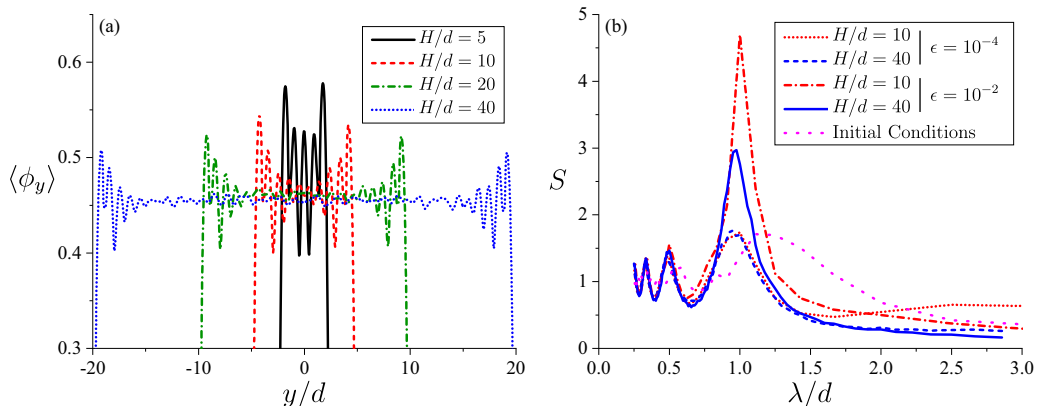


FIG. 11. Data on the suspension microstructures from simulations for $\phi_A = 0.45$ are shown. (a) The local areal fraction as a function of position, y , is shown as a function of confinement ratios, H/d , between 5 and 40 for $\epsilon = 10^{-2}$. (b) The structure factors S as a function of the wave number $\lambda = 2\pi/q_y$, in the gradient direction are compared for $H/d = 10$ and 40 and $\epsilon = 10^{-4}$ and 10^{-2} . The structure factor corresponding to the initial condition for $H/d = 10$ is also shown.

Figure 11(a) shows, for the rougher particles ($\epsilon = 10^{-2}$), that the local areal fraction is highly organized at $H/d = 5$ throughout the gap, with the particles forming layers that are aligned in the flow direction. For $H/d > 5$, the particles remain highly organized and aligned with the flow direction near the bounding walls, but appear to be less organized near the center of the gap as H/d increases. However, the rough particles do remain organized and aligned in the flow direction even far from the bounding walls. To demonstrate this clearly, Fig. 11(b) compares the structure factor S at confinements of $H/d = 10$ and 40. The structure for $\epsilon = 10^{-2}$ exhibits a strong correlation at a spacing of one particle diameter at both confinements, reinforcing the idea that layering occurs, though it does not appear as regular for $H/d = 40$. The microstructure is not sensitive to confinement if $H/d \geq 10$ for particles far from the walls, as shown in Sec. S3 [24]. Therefore, the difference between the structure factors for small ($H/d = 10$) and large ($H/d = 40$) gaps is due to a larger fraction of the highly ordered layers near the walls in the narrower channel.

Figure 11(b) also compares structures for the smooth and rough particles. At the same spacing of the bounding walls, the smoother particles are seen to be less organized, as indicated by the smaller amplitude of S at the wavelength $\lambda = d$. This amplitude is comparable with that of the random initial distribution shown by the dotted line in 11(b) (the structure factor of the initial conditions exhibits a small peak at $\lambda \approx d$ due to the excluded-volume interactions between the particles). Note also that, unlike the rough particles, the structure factors of suspensions of smooth particles are not sensitive to the gap width, which indicates that even near walls organization of the smooth particles is much weaker (see Sec. S3 [24] for additional details). Consequently, the diffusivity of the smoother particles remains higher than that of the rougher particles (see Fig. 10) regardless of the degree of confinement since the smoother particles experience more irreversible contacts.

Figure 12(a) compares diffusivities across a wide range of concentrations for unbounded (periodic) and bounded ($H/d = 10$) suspensions of rough and smooth particles. The same trend is seen for the unbounded system as for the bounded one: diffusivities are larger for the rougher particles at small concentrations but are smaller at high areal fractions. Whether bounding walls are present or not, roughness promotes particle layering and an associated reduction in diffusion. Figure 12(b) confirms, for the case of $\phi_A = 0.45$, that layering occurs more strongly for particles of roughness $\epsilon = 10^{-2}$ versus $\epsilon = 10^{-4}$. Furthermore, even though the structure factor S for rough particles in a bounded system exhibits some dependence on the gap width H , it approaches S of the unbounded system for a sufficiently large gap ($H = 40d$); see also Sec. S3.A [24].

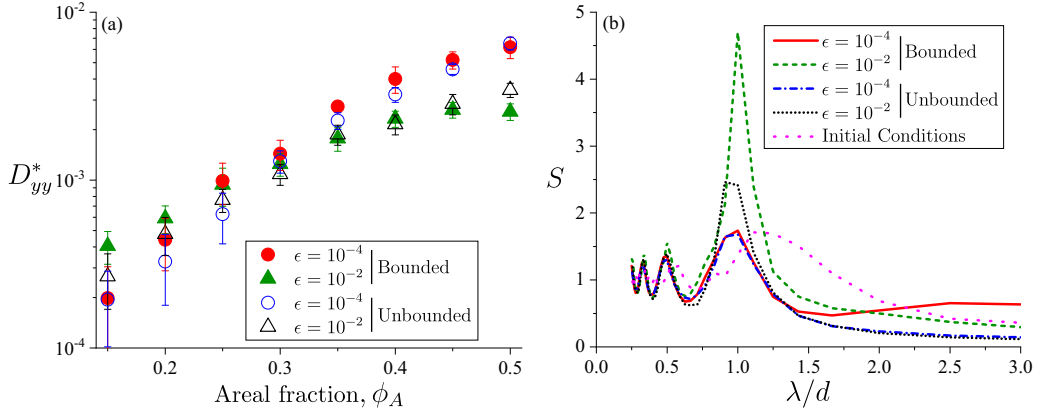


FIG. 12. (a) Diffusion coefficient calculated from monolayer simulations is plotted as a function of ϕ_A for unbounded (periodic) and bounded ($H/d = 10$) systems for two values of roughness, ϵ . (b) Structure factors S in the unbounded and bounded systems for $\phi_A = 0.45$ and $H/d = 10$; λ is the wave number in the gradient direction. For comparison, the structure factor corresponding to the initial condition for the bounded system is also shown.

3. Polydispersity

To investigate a means of disrupting particle layering and the effects on the diffusivities of rough and smooth particles, a nonmonodisperse size distribution was simulated. The particle diameters (d_i , $i = 1$ to N) were selected from a normal distribution with mean size d and standard deviation σ , though diameters smaller than $0.1d$ and larger than $2.5d$ were rejected.

Figure 13(a) shows the diffusivities $D_{yy}^* = D_{yy}/\dot{\gamma}d^2$ calculated using the mean diameter d for $\phi = 0.45$. For the rough particles, the diffusivity increases with polydispersity and approaches the diffusivities computed for smooth particles which remain relatively constant with respect to σ . Changes in the microstructure with polydispersity and roughness, as shown in Fig. 13(b), can explain the relative values of the diffusivities. For rough particles, the structure is relatively unorganized for polydisperse ($\sigma = 0.4d$) versus monodisperse ($\sigma = 0$) size distributions. The latter case exhibits regular oscillations with a period corresponding to the mean diameter d , whereas the oscillations are disrupted by the wide distribution of particle sizes for the polydisperse case. The bulk areal fraction profile of smoother particles ($\epsilon = 10^{-4}$) suggests that they are also less organized

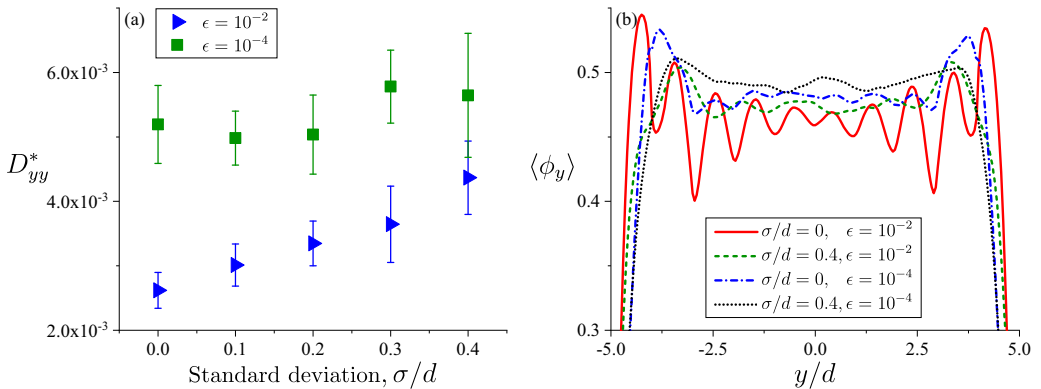


FIG. 13. Results from monolayer simulations are shown for $\epsilon = 10^{-2}$ and 10^{-4} , an areal fraction of $\phi_A = 0.45$, and $H/d = 10$. (a) Dimensionless diffusion coefficient as a function of polydispersity, which is quantified by the standard deviation σ of the particle diameters. (b) Average local areal fraction profile for $\sigma = 0$ and $0.4d$.

upon increasing polydispersity. However, the angular distribution function $g(\theta; \delta)$ shown in Fig. S7 [24] indicates that the polydispersity has a negligible effect on their microstructure near contact. Hence the polydispersity has little effect on the diffusivities of sufficiently smooth particles.

VI. DISCUSSION AND CONCLUSIONS

Evidence presented here indicates that two regimes of shear-induced diffusivity exist: when compared to smooth particles, rougher particles diffuse more rapidly at low concentration and less rapidly at high concentrations. The former result is consistent with models of diffusion in the limit of dilute concentrations [23], where contacts between larger asperities on the surface of rougher spheres drive larger net displacements of the particles during collisions. However, the dependence of diffusivity on the roughness reverses at a volume fraction of approximately 0.25 and the smoother particles become more diffusive than roughened ones. For these larger concentrations, numerical investigations have revealed that rough particles tend to organize into successive layers oriented parallel to the flow. Consequently, rough particles collide and diffuse less than the smooth particles, which remain relatively disorganized.

Numerical studies also predict that particle diffusivity, as well as the organization into layers, is independent on the level of confinement for gaps of size $H/d \geq 10$. Sufficient polydispersity of the particle size distribution decreases the organization of the particles into layers at large volume fractions, thus suppressing the effect of particle roughness on diffusivity.

The nonuniform dependence of diffusivity on particle roughness at high and low concentrations may help account for the large discrepancies reported in the literature, as seen in Fig. 1. Large variations in the roughness can cause differences of a factor of two or more in the diffusion coefficient. Furthermore, rougher particles previously would have been assumed to give consistently higher diffusivities, but in fact there should be a crossover in the relative values of the diffusivities for rough versus smooth particles at intermediate volume fractions of around 0.25.

The simulations qualitatively predict the unexpectedly lower diffusivities at large ϕ for rougher particles using a simple description of the particle interactions. However, the quantitative values for the measured and predicted diffusivities differ considerably; there is a factor of ≈ 4 difference at $\phi = 0.25$ and ≈ 6 at $\phi = 0.35$. Continuing work will add complexity to the model to better align the quantitative values of the predictions with the experimental measurements. Additional components of lubrication interactions and frictional contacts [36] will be included; the latter effect can increase shear-induced diffusivities by large factors according to the simulations of Gallier [37]. These simulations will be used to further investigate the relationship between structure, roughness, and diffusivity.

Microstructural changes in non-Brownian suspensions have long been recognized to dramatically influence their rheology. The strong interplay between microstructure and rheology is evidenced for instance by changing the macroscopic flow field, as with shear reversal and oscillatory flows [34,38–40]. Remarkably, the results presented here show that the microstructure can also be altered by microscopic changes occurring at the scale of particle contacts. When changing the particle roughness, the suspension is more likely to organize into layers, particularly at high concentrations. The interplay of particle interactions over short ranges (i.e., roughness) and microstructure must therefore be considered when evaluating dynamic quantities, such as the shear-induced diffusivity, in addition to the rheology of the suspensions.

ACKNOWLEDGMENTS

Acknowledgment is made to the donors of the American Chemical Society Petroleum Research Fund for partial support of this research through Grant No. 61501-ND9. This work was also partially supported by ANR *ScienceFriction* (Grant No. ANR-18-CE30-0024).

- [1] E. Eckstein, D. Bailey, and A. Shapiro, Self-diffusion of particles in shear flow of a suspension, *J. Fluid Mech.* **79**, 191 (1977).
- [2] D. Leighton and A. Acrivos, Measurement of shear-induced self-diffusion in concentrated suspensions of spheres, *J. Fluid Mech.* **177**, 109 (1987).
- [3] M. Lopez and M. Graham, Enhancement of mixing and adsorption in microfluidic devices by shear-induced diffusion and topography-induced secondary flow, *Phys. Fluids* **20**, 053304 (2008).
- [4] L. Wang, D. Koch, X. Yin, and C. Cohen, Hydrodynamic diffusion and mass transfer across a sheared suspension of neutrally buoyant spheres, *Phys. Fluids* **21**, 033303 (2009).
- [5] B. Metzger, O. Rahli, and X. Yin, Heat transfer across sheared suspensions: Role of the shear-induced diffusion, *J. Fluid Mech.* **724**, 527 (2013).
- [6] M. Souzy, X. Yin, E. Villermaux, C. Abid, and B. Metzger, Super-diffusion in sheared suspensions, *Phys. Fluids* **27**, 041705 (2015).
- [7] D. Leighton and A. Acrivos, The shear-induced migration of particles in concentrated suspensions, *J. Fluid Mech.* **181**, 415 (1987).
- [8] G. Drazer, J. Koplik, B. Khusid, and A. Acrivos, Microstructure and velocity fluctuations in sheared suspensions, *J. Fluid Mech.* **511**, 237 (2004).
- [9] F. Gadala-Maria and A. Acrivos, Shear-induced structure in a concentrated suspension of solid spheres, *J. Rheol.* **24**, 799 (1980).
- [10] A. Acrivos, Bingham Award Lecture - 1994 Shear-induced particle diffusion in concentrated suspensions of noncolloidal particles, *J. Rheol.* **39**, 813 (1995).
- [11] S. Sinton and A. Chow, NMR flow imaging of fluids and solid suspensions in Poiseuille flow, *J. Rheol.* **35**, 735 (1991).
- [12] C. Koh, P. Hookham, and L. Leal, An experimental investigation of concentrated suspension flows in a rectangular channel, *J. Fluid Mech.* **266**, 1 (1994).
- [13] V. Breedveld, D. van den Ende, M. Bosscher, R. J. J. Jongschaap, and J. Mellema, Measurement shear-induced self-diffusion in counterrotating geometry, *Phys. Rev. E* **63**, 021403 (2001).
- [14] V. Breedveld, D. van den Ende, A. Tripathi, and A. Acrivos, The measurement of the shear-induced particle and fluid tracer diffusivities in concentrated suspensions by a novel method, *J. Fluid Mech.* **375**, 297 (1998).
- [15] V. Breedveld, D. Van Den Ende, M. Bosscher, R. Jongschaap, and J. Mellema, Measurement of the full shear-induced self-diffusion tensor of noncolloidal suspensions, *J. Chem. Phys.* **116**, 10529 (2002).
- [16] I. Zarraga and D. Leighton, Measurement of an unexpectedly large shear-induced self-diffusivity in a dilute suspension of spheres, *Phys. Fluids* **14**, 2194 (2002).
- [17] A. Sierou and J. Brady, Shear-induced self-diffusion in non-colloidal suspensions, *J. Fluid Mech.* **506**, 285 (2004).
- [18] P. Arp and S. Mason, The kinetics of flowing dispersions: IX. Doublets of rigid spheres (experimental), *J. Colloid Interface Sci.* **61**, 44 (1977).
- [19] I. Rampall, J. R. Smart, and D. T. Leighton, The influence of surface roughness on the particle-pair distribution function of dilute suspensions of non-colloidal spheres in simple shear flow, *J. Fluid Mech.* **339**, 1 (1997).
- [20] F. Blanc, F. Peters, and E. Lemaire, Experimental Signature of the Pair Trajectories of Rough Spheres in the Shear-Induced Microstructure in Noncolloidal Suspensions, *Phys. Rev. Lett.* **107**, 208302 (2011).
- [21] P. Pham, B. Metzger, and J. E. Butler, Particle dispersion in sheared suspensions: Crucial role of solid-solid contacts, *Phys. Fluids* **27**, 051701 (2015).
- [22] P. Pham, J. E. Butler, and B. Metzger, Origin of critical strain amplitude in periodically sheared suspensions, *Phys. Rev. Fluids* **1**, 022201(R) (2016).
- [23] F. R. Da Cunha and E. Hinch, Shear-induced dispersion in a dilute suspension of rough spheres, *J. Fluid Mech.* **309**, 211 (1996).
- [24] See Supplemental Material at <http://link.aps.org/supplemental/10.1103/PhysRevFluids.8.064303> for (1) comparison of simulations using the simplified suspension model employed in the current work with simulations that employ more detailed models, (2) data on scaling of the mean-squared displacement with

- respect to time, (3) additional data on suspension microstructure, (4) microstructure of the polydisperse system, and (5) information on image analysis and particle detection, which includes Refs. [41–44].
- [25] M. Zurita-Gotor, J. Bławdziewicz, and E. Wajnryb, Swapping trajectories: A new wall-induced cross-streamline particle migration mechanism in a dilute suspension of spheres, *J. Fluid Mech.* **592**, 447 (2007).
 - [26] K. Yeo and M. R. Maxey, Anomalous diffusion of wall-bounded non-colloidal suspensions in a steady shear flow, *Europhys. Lett.* **92**, 24008 (2010).
 - [27] G. K. Batchelor and J. T. Green, The hydrodynamic interaction of two small freely-moving spheres in a linear flow field, *J. Fluid Mech.* **56**, 375 (1972).
 - [28] B. Metzger, P. Pham, and J. E. Butler, Irreversibility and chaos: Role of lubrication interactions in sheared suspensions, *Phys. Rev. E* **87**, 052304 (2013).
 - [29] B. Metzger and J. E. Butler, Irreversibility and chaos: Role of long-range hydrodynamic interactions in sheared suspensions, *Phys. Rev. E* **82**, 051406 (2010).
 - [30] A. Lees and S. Edwards, The computer study of transport processes under extreme conditions, *J. Phys. C* **5**, 1921 (1972).
 - [31] F. Blanc, E. Lemaire, A. Meunier, and F. Peters, Microstructure in sheared non-Brownian concentrated suspensions, *J. Rheol.* **57**, 273 (2013).
 - [32] K. Yeo and M. Maxey, Dynamics of concentrated suspensions of non-colloidal particles in Couette flow, *J. Fluid Mech.* **649**, 205 (2010).
 - [33] S. Gallier, E. Lemaire, L. Lobry, and F. Peters, Effect of confinement in wall-bounded non-colloidal suspensions, *J. Fluid Mech.* **799**, 100 (2016).
 - [34] J. M. Bricker and J. E. Butler, Correlation between stresses and microstructure in concentrated suspensions of non-Brownian spheres subject to unsteady shear flows, *J. Rheol.* **51**, 735 (2007).
 - [35] I. E. Zarraga, D. A. Hill, and D. T. Leighton, Jr., The characterization of the total stress of concentrated suspensions of noncolloidal spheres in Newtonian fluids, *J. Rheol.* **44**, 185 (2000).
 - [36] R. Mari, R. Seto, J. F. Morris, and M. M. Denn, Shear thickening, frictionless and frictional rheologies in non-Brownian suspensions, *J. Rheol.* **58**, 1693 (2014).
 - [37] S. Gallier, Simulation numérique de suspensions frictionnelles. Application aux propergols solides, Ph.D. thesis, Université Nice Sophia Antipolis, 2014.
 - [38] J. M. Bricker and J. E. Butler, Oscillatory shear of suspensions of noncolloidal particles, *J. Rheol.* **50**, 711 (2006).
 - [39] V. G. Kolli, E. J. Pollauf, and F. Gadala-Maria, Transient normal stress response in a concentrated suspension of spherical particles, *J. Rheol.* **46**, 321 (2002).
 - [40] F. Blanc, F. Peters, and E. Lemaire, Local transient rheological behavior of concentrated suspensions, *J. Rheol.* **55**, 835 (2011).
 - [41] G. Bradski, The OpenCV library, Dr. Dobb's J. Software Tools **25**, 120 (2000).
 - [42] S. van der Walt, J. L. Schönberger, J. Nunez-Iglesias, F. Boulogne, J. D. Warner, N. Yager, E. Gouillart, T. Yu, and the scikit-Image contributors, Scikit-image: image processing in Python, *PeerJ* **2**, e453 (2014).
 - [43] J. C. Crocker and D. G. Grier, Methods of digital video microscopy for colloidal studies, *J. Colloid Interface Sci.* **179**, 298 (1996).
 - [44] D. B. Allan, T. Caswell, N. C. Keim, C. M. van der Wel, and R. W. Verweij, Trackpy: v0.6.1, doi:10.5281/zenodo.7670439.